Cislunar Initial Orbit Determination Using Sensor and Measurement-Centric Admissible Regions

Queenique Dinh
University of Colorado Boulder
Daniel J. Scheeres & Marcus J. Holzinger
University of Colorado Boulder

ABSTRACT

With the expansion of human activities in cislunar space, it is crucial to augment space situational awareness (SSA) capabilities across the region. Adapting initial orbit determination (IOD) techniques is a key opportunity, addressing challenges like the chaotic dynamics of the circular restricted 3-body problem (CR3BP) and the spatial scales between targets and observers which ultimately cause traditional IOD techniques to fail. This work leverages admissible regions theory and topocentric intersection theory analysis to develop an IOD method for objects in cislunar space. Topocentric intersection theory analysis (TITA) links two observations by looking at lower dimensional projections of their admissible regions in measurement and sensor-centric coordinates, then identifying the potential initial range and range-rates at the intersections of these projections. When considering the effects of uncertainty on both measurements, the points of intersections turn into areas, and we observe a shift in their locations on the initial range and range-rate plane. We apply the work to three orbits of interest around the L2 Lagrange point - a planar orbit, a 3:1 resonance Halo orbit, and a 9:2 resonance Near-Rectilinear Halo Orbit - and discuss some of its benefits and limitations. By conducting this exploration of the solution space, we set the foundation for systematically defining admissible regions for cislunar IOD.

1. INTRODUCTION

As interest in utilizing cislunar space continues to grow, there is also a growing need to augment space situational awareness (SSA) capabilities. One opportunity is expanding on Initial Orbit Determination (IOD) techniques and adapting them for the challenges of the domain, particularly of the Circular Restricted 3-Body Problem (CR3BP) - the dynamical system often used to study cislunar space. The CR3BP exhibits chaotic, non-integrable dynamics and lacks analytical solutions like those in Keplerian dynamics; this results in a high dependency on numerical computation to analyze the motion of space objects. In addition, the spatial scale of the domain restricts observations of space objects to those from optical telescopes. Optical observations provide angle and angle-rate information at most, leaving the range and range-rate undefined along the line of sight. Traditional IOD techniques fail with these observations due to the lack of curvature information and their underlying assumptions of two-body dynamics [1], a phenomenon referred to as the Too-Short Arc Problem [2].

Admissible regions theory, developed in [2], addresses the Too-Short Arc problem by maximizing the information extracted from optical observations through hypothesized constraints on the solution space. The constraints bound the initially infinite two-dimensional plane of range and range-rates that might complete the state vector to a compact subset in which the solution may be more efficiently found. Constraints on the admissible region are generated from a priori information about the object, and are based on any number of characteristics. For example, dynamical constraints can restrict objects based on whether they are in heliocentric or geocentric orbits. Geometric constraints could exclude the closest or furthest approaches from the primary attracting body, or put limitations on orbital shape. Observational constraints might include the brightness of the object, eliminating ranges that prevent the object from being detected in the first place. The final admissible region, then, is the intersection of all applied constraints.

Potential constraints on the admissible region are non-unique and are applied as needed depending on the problem at hand. Although first developed in [2] for heliocentric objects, extensive work has since developed similar constraints

for geocentric objects [3, 4] and even space-based observers in near-Earth orbits [5]. More recent work leverages admissible regions theory to advance IOD techniques for cislunar space, specifically constraining the solution space such that approaches like optimization [6] or filtering are primed to converge [7]. When considering applicable constraints on admissible regions for cislunar space, extensions include those based on observation capabilities and some dynamical constraints. For example, we can exclude objects that may escape the Earth-Moon region and the CR3BP dynamics.

One less obvious extension from two-body to three-body dynamics is how to define applicable geometric constraints. When analytical solutions exist, objects are eliminated easily based on geometric qualities like eccentricity, periapsis or apoapsis, or inclination. These quantities are not as readily defined in cislunar space because computational analysis is necessary. An object would need to be propagated to determine whether it collides with the Earth or the Moon, for example, and finding such a collision for any particular trajectory is not always guaranteed. With the spatial scales of cislunar space, the potential constraints that can be extended still result in relatively large admissible regions. Thus, there is an opportunity to develop more generalized and applicable constraints for multi-body dynamical systems like the CR3BP.

This work aims to address the opportunity of defining such constraints by seeking to understand the possible ways of connecting two measurements in the solution space. We take a measurement and sensor-centric approach to admissible regions in the CR3BP, thus aligning our understanding with how we receive information from optical measurements. Ultimately, a visual method of IOD using lower dimensional projections of the admissible region is developed. We use simulated measurements from three sample orbits and discuss the existence of ambiguous solutions and their effects. The work also serves as a method of initializing guesses for more robust IOD techniques, allowing for more efficient use of current algorithms, and sets the foundation for defining applicable geometric constraints for admissible regions in the CR3BP.

2. IMPLEMENTATION

The foundation of this work lies in admissible regions theory, first presented in [2] as a method of maximizing the information that can be extracted from an attributable vector. The attributable vector summarizes the information available from optical observations, containing two angles and two angle-rates,

$$\mathscr{A} = \left(\theta, \dot{\theta}, \phi, \dot{\phi}\right) \in [-\pi, \pi) \times \left(-\frac{\pi}{2}, \frac{\pi}{2}\right) \times \mathbb{R}^2 \tag{1}$$

This vector leaves the range and range-rate undefined, which initially lie in an infinite 2D plane. Admissible regions theory reduces the infinite 2D plane of range and range-rate to a compact subset by imposing constraints on the solution space based on a priori information. This region is then finitely sampled to define a field of hypothesized objects, referred to in [2] as virtual asteroids and generally referred to as virtual objects. Full 6-element state vectors are created by completing the 4-element attributable vector with a hypothesized range and range-rate sampled from the compact subset. After propagating the virtual objects, they are compared to another known observation and linked according to a metric, like the attribution penalty discussed in [8]. The intention is to determine whether one of the hypothesized objects represents the actual object. In linking two observations to the same object, an initial estimation of the state vector is simultaneously provided. Thus, observation linkage and initial orbit determination are related problems.

Later work develops this theory further through something called Intersection Theory Analysis (ITA), specifically in [9] for geocentric observations. Intersection Theory Analysis relies on the Theory of General Position, which gives the dimension of an intersection d as

$$d = (k+l) - n \tag{2}$$

For this problem, the variables k and l equal two for the dimension of the range and range-rate planes [10]. These planes are generated by initializing admissible regions at the epochs of two measurements, then propagating them to the same epoch for comparison. The remaining variable n is the 6-dimensional space of the state variables, resulting in $d = -2$. Since $d < 0$, the two planes cannot intersect coincidentally and thus, any intersection of two range and range-rate planes means that the two respective measurements are linked. Furthermore, the intersection point provides the orbit estimate for the linked observations. In [9], intersections are found by first conducting a one-to-three mapping of the two-dimensional admissible region to three two-dimensional projective spaces. This simplifies the visualization

of how two admissible regions can overlap. The mutual overlap in all three projective spaces yields the solution to the linkage and initial orbit determination problems.

The work in [9] also briefly introduces the concept of Topocentric Intersection Theory Analysis (TITA), where the search for admissible region intersections is done specifically in the observation space. The choice of coordinate space often results in its own set of advantages. For example, [9] uses canonical element sets like the Delaunay or Hamiltonian elements for their integral invariant properties. The work in [10] opts to use the Poincaré orbit element space for its lack of nonsingularities. Using the topocentric observation geometry simplifies the intersection search process because of degeneracy in the projective spaces. There may be a drawback, though, in the computational load due to the number necessary coordinate transforms between the Cartesian and topocentric spaces to propagate the dynamics and conduct the analysis.

This paper discusses the implementation of Topocentric Intersection Theory Analysis for the CR3BP dynamics of cislunar space. The choice to conduct ITA in topocentric observation coordinates is to develop a measurement and sensor-centric view on the IOD problem, such that our understanding and intuition of the solution space is aligned with how we receive observations. The computational load is mitigated by opting to propagate the dynamics in a spherical form of the CR3BP equations, eliminating the need to transform between spherical and Cartesian coordinates. The field of virtual objects is generated at an initial measurement epoch and propagated to the final measurement epoch, which is chosen as the time for comparison. This eliminates the need to generate and propagate a second field of virtual objects.

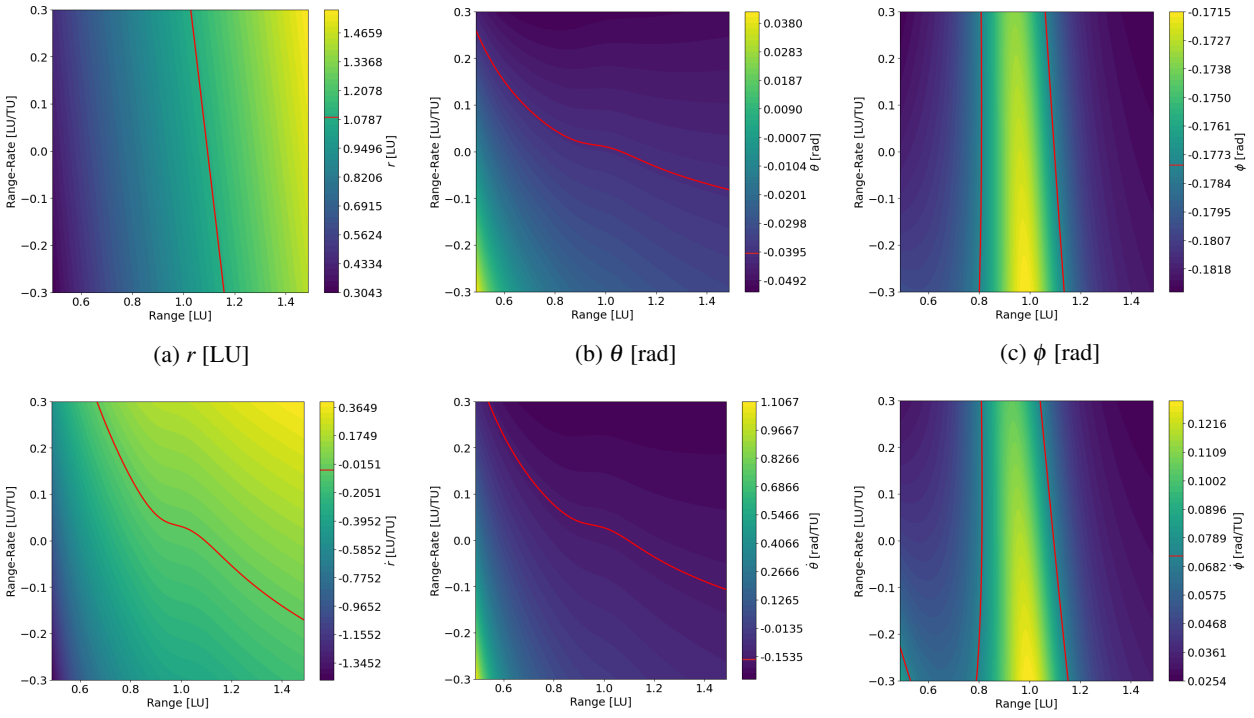

(a) r [LU] (b) θ [rad] (c) ϕ [rad]

(d) $\dot{r}$ [LU/TU] (e) $\dot{\theta}$ [rad/TU] (f) $\dot{\phi}$ [rad/TU]

Fig. 1: Contour plots representing propagated values for all state variables from initial measurement epoch to final measurement epoch. Highlighted contour line represents set of initial range and range-rates which produce the correct value for each state variable.

We first develop the Topological ITA procedure on a general sample orbit, before later detailing the observation scenarios of interest and presenting specific results. Two perfect measurements of a space object are assumed, each yielding an attributable vector consisting of angles and angle-rates. These measurements are taken from the barycenter of the Earth-Moon CR3BP, for simplicity, to eliminate relative motion between the target and the observer. We also assume no line-of-sight constraints. Thus, there are eight pieces of information to define the initial range and range-rate. To generate the field of virtual objects, we survey over a grid of range and range-rate values, linearly sampling

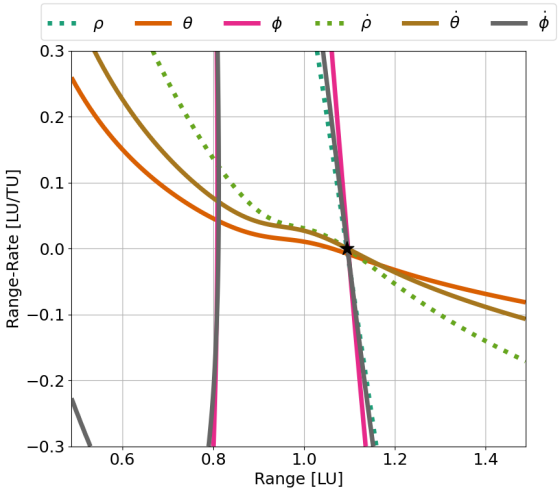

Fig. 2: Composite plot of state variable contour lines from Fig. 1

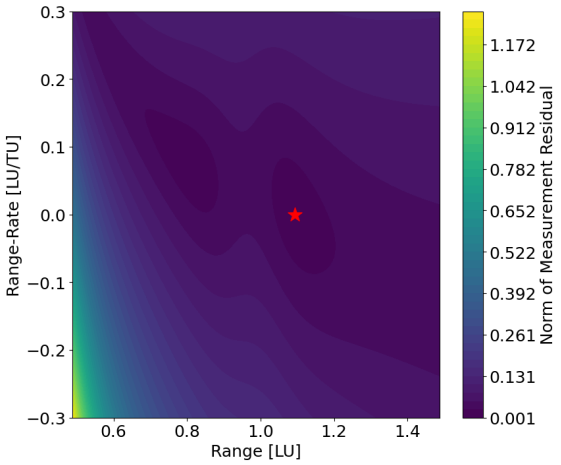

Fig. 3: Contour plot of measurement residual at final measurement epoch.

100 values in each direction. For range values, we choose a bound centered about the location on the x-axis of the Moon in the CR3BP, with 0.5 LU on each side. For range-rate values, we choose values between -0.3 and 0.3 LU/TU. These values are chosen to be overly conservative to study a broad swath of the potential solution space, while also keeping in mind the necessary computational load. This grid sampling results in 10000 virtual objects, with initial states generated using the first attributable vector and each hypothesized range and range-rate pair. Each of these objects has the same probability of representing the true object, but we have not yet determined which is closest. This field is then propagated to the epoch of the final measurement and compared to its attributable vector.

Fig. 1 shows the results of propagating the field of virtual objects from the initial measurement epoch to the final measurement epoch, where the horizontal and vertical axes represent the hypothesized initial range and range-rate, respectively. By looking across the six contour plots for any virtual object, the full state vector after propagation can be constructed. We observe smooth contours for all state variables. Since this is a simulated scenario, we have the full true state vector of the object at the final measurement epoch, whereas with an attributable vector, we would only know the angles and angle-rates. Using the known information at the final epoch, for each state variable contour plot, we highlight the set of initial range and range-rates that results in the true value of the variable after propagation. We see that for the in-plane angle θ and its corresponding rate, we have one line of values that when propagated will yield the true θ and $\dot{\theta}$ value. The same behavior is seen for the range and range-rate values, although we would not normally have access to this information. For the out-of-plane angle, though, we see several lines. It is possible that these lines are part of one or more continuous curves, although it is unclear due to the chosen initial range and range-rate bounds. Each angle contour line appears to have similar behavior to its corresponding angle rate, but as pairs appear to be transverse to each other.

The highlighted contour lines are lower dimensional projections of the resultant admissible region, showing the sets of potential range and range-rates. When we take a composite of these contour lines, as seen in Fig. 2, we see that the true solution marked by the black star is at the intersection of all lines. This behavior aligns with our expectations, as the two simulated measurements are known to be linked. Thus, there should be a point in the range and range-rate space mutual to all projections. The intersection occurs both when considering the projections from all six state variables, and when considering just the projections from the measured variables. The projections from range and range-rate are shown as dotted lines because we would not normally have access to this information, whereas the measured variables are shown as solid.

The composite plot in Fig. 2 visually demonstrates a form of topocentric intersection theory analysis, as it shows where the projections of the admissible region intersect. It is less trivial, however, to isolate this intersection point numerically, which would require comparisons along each of the highlighted contour lines to find the mutual set of range and range-rate values. We instead look at the measurement residual at the final measurement epoch, specifically the L2-norm of the residual vector between the true attributable $\mathscr{A}_f$ and the predicted attributable $\mathscr{A}_{f,p}$. This value

shows us the same information we are interested in from the composite plot, which is the initial range and range-rate values resulting in the measured values after propagation. If a particular range and range-rate pair does reflect the true object, the norm of the measurement residual should approach zero. An example of a contour plot showing the norm of the measurement residual vector for each virtual object is shown in Fig. 3. The true initial range and range-rate for the sample case is marked with a red star; we see that it lies within one of the darkest regions of the contour, indicating a minimum value.

Upon closer inspection, there also appears to be a secondary local minimum in Fig. 3, located in front of the Moon's location along the range direction and with slightly higher range-rate values. Without explicitly inspecting the values in this local minimum, it is difficult to discern whether the minima are of similar depths, which may present a problem when using the numerical minima of the contour to find the mutual intersection of the admissible region projections. When comparing the contour plot to the composite plot, it appears the secondary minima corresponds to a segment where the out-of-plane angle and angle-rate overlap, and the in-plane angle and angle-rate are relatively close. Because the measurement residual contour is generated using an L2-norm of these values, areas where the lines almost overlap but not quite will also start to approach zero, especially depending on the discretization of the sample grid. We consider this ambiguity as we study additional observation scenarios in this work, and emphasize that this ambiguity is due to the lack of range and range-rate information. For example, had we considered the residual to be the norm of the difference between the full state vectors, there would not be a secondary minimum as all six contour lines only intersect unambiguously at one point. Additional analysis also shows that this ambiguous solution lies along the line of sight from the observer to the target.

2.1 Simulated Observation Scenarios

For this work, three orbits are chosen from the L2 Southern Halo family for their differing characteristics. The first is the planar orbit connecting the L2 Planar Lyapunov and Halo families [11], to serve as an edge case for analysis due to its lack of out-of-plane motion. The other orbits are chosen for operational interest due to their synodic resonances, including a 9:2 Near-Rectilinear Halo Orbit (NRHO) modeled after the one chosen for NASA Lunar Gateway [12] and a 3:1 Halo orbit. The periods and Jacobi constants of these orbits are shown in Table 1, and the orbits themselves are plotted in the Cartesian space in Fig. 4.

Table 1: Parameters for orbits of interest in the L2 Southern Halo Family.

Orbit	Period [LU]	Jacobi Constant
Planar	3.4155	3.1521
Halo (3:1 Resonance)	2.2667	3.0157
Near-Rectilinear (9:2 Resonance)	1.5094	3.0465

The simulated observer is placed at the origin, or the mutual barycenter, of the Earth-Moon system for simplicity to eliminate relative motion between targets and observers. We assume line of sight at all times and do not consider occlusion, brightness, or other factors related to observational capabilities. Simulated observations are generated by first transforming a Cartesian initial state vector into the spherical frame. Then, because a spherical form of the CR3BP equations is used in this work, additional observations are easily generated by taking the angles and angle-rates from the object's propagated trajectory. The measured variable θ is the in-plane angle between the primaries and the object and the variable ϕ is the out-of-plane angle between the plane of the primaries and the object. For each observation scenario, we assume two measurements which both give attributable vectors. The time between these measurements is variable with a value of 6, 12, or 24 hours. To limit the number of cases being presented, four points are chosen along each orbit as initial conditions, spaced equally in time based on the orbital period. Thus, the two measurements are the chosen initial point of four along the orbit and the state vector 6, 12, or 24 hours later.

Fig. 4 shows all pairs of initial and final measurements by representing the initial points with circular markers and the final points with diamond markers. The circular markers become lighter as the time along the orbit increases, while the diamond markers become lighter as the time between the initial and final measurement increases. Each circular marker is associated with the following three diamond markers along the orbit. Thus, each pair of circular and diamond marker represents the Cartesian location of the space object at the initial and final measurement time for every observation scenario in this work. We assume, at first, that these measurements are perfect with no uncertainty; the effects of uncertainty are discussed later in Section 3.1.

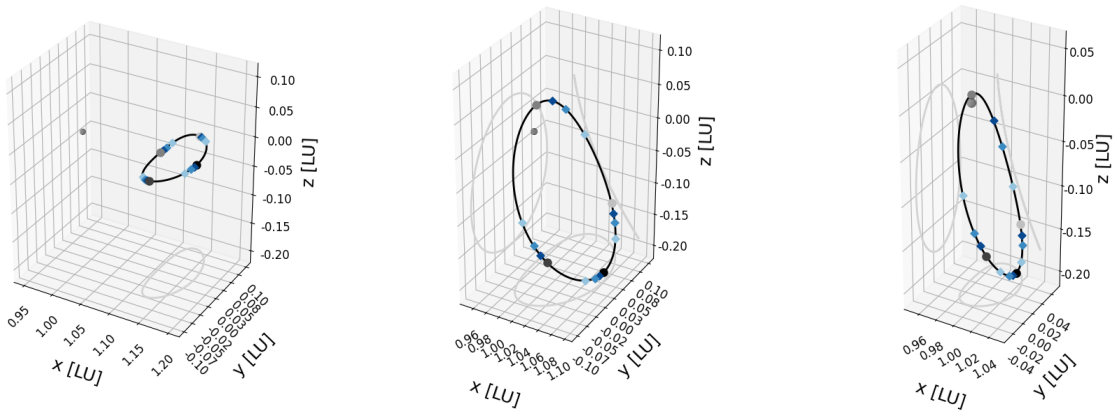

(a) Planar (b) Halo (3:1 Resonance) (c) NRHO (9:2 Resonance)

Fig. 4: Orbits of interest in Cartesian space. Circular markers represent chosen initial points along orbit, with values of 0, 0.25, 0.5, and 0.75 of the orbit's period from darkest to lightest marker. Diamond markers represent chosen measurement intervals relative to each initial point, where the times are 6, 12, or 24 hours later from darkest to lightest marker.

Studying this variety of observation scenarios informs us of the expected behavior when adjusting different parameters. By doing so, we gain a broader understanding of the solution space which may lead to ways of better defining generalized admissible regions and relevant constraints for the cislunar domain.

3. RESULTS AND ANALYSIS

The results for the orbits of interest in this work are in the Appendix in Section 7. The first set of figures for each orbit shows the composite plots of the admissible region projections, as seen in Fig. 2, organized in rows by initial location along the orbit and in columns by time between measurements. The second set of figures is the contour of the measurement residual norm, as seen in Fig. 3, organized in the same manner.

One pattern among the composite figures is how the contour lines corresponding to the measured variables (the solid lines) do not appear to intersect perfectly for all scenarios. Specifically, the intersection with all four of the measured variables at the true initial range and range-rate is not guaranteed as the time between measurements decreases. This is due to a numerical limitation in this approach. With shorter time spans, the spread in resulting variable values after propagation is reduced. For example, the difference between the minimum and maximum of a particular variable value grid may be in the tenths or hundredths. So when isolating the contour line associated with the measured variable value at the final epoch, interpolation over the grid causes the lines to shift, especially when considering numerical precision. As the time between measurements increases - and thus the resulting spread of variable values increases - the highlighted contour line is more concise, bringing the intersection more clearly into focus. This pattern is most clearly observed with the Halo orbit results in Fig. 6 and the NRHO results in Fig. 18.

The numerical limitations of the composite plot generation, along with the chaotic and unstable CR3BP dynamics near L2, are also the likely reasons for the discrepancies in the NRHO results. We observe that not all measured variables are actually visible in the results for all observation scenarios. For example, looking at the row corresponding to 0.75 of the orbital period, none of the measured variables appear on the plot with six hours between measurements. Then even as the time between measurements increases, only the out-of-plane angle-rate $\dot{\phi}$ appears and in a single vertical line.

The resulting composite plots for the planar orbit scenarios have their own standout characteristics. While we still see a refinement of the intersection point at the true initial range and range-rate as the time between measurements increases, we also see denser collections of the contour lines towards the center of the plots. This behavior is especially obvious in the last column of results, where the overlapping lines are indistinguishable from each other. The likely reason is the degenerate viewing geometry for a planar orbit. Without an out-of-plane component, the line of sight

could intersect multiple points that return the same measurement, despite having different range and range-rate values. Upon closer inspection, the clusters of contour lines contain all measured variables except for the in-plane angle θ. While the ambiguity of the out-of-plane angle ϕ is trivial, an interesting observation is how the degenerate viewing geometry also affects the angle-rates. From the results of the planar orbit, we conclude that relative viewing geometry between targets and observers can also be a limitation for TITA.

As discussed with the sample scenario presented in Section 2, there exist ambiguous solutions when considering the intersections of just the four measured variables. For several of the observation scenarios presented, we observe clear secondary intersections occurring in front of the Moon's location in the range direction. In other cases, we observe regions where two or more of the measured variables intersect, while the remaining ones are in the relatively near vicinity. The secondary and close intersections correspond to local minima in the contours of the measurement residual norm. This presents a challenge in defining the initial range and range-rate because an erroneous value may be returned when taking the numerical minima. Thus, additional constraints on the solution space should be considered to further refine the solution. Imposing constraints would likely be most effective in the scenarios with detached local minima, but other approaches will need to be considered for the scenarios where the minima have different structures. For example, we see a relative lack of clear minima entirely for the planar case. For the halo cases, we see U-shaped curves or even vertical lines where the minima are located, indicating a greater need for bounds on the range-rate space.

3.1 Considering Measurement Uncertainty

The likelihood of an erroneous result due to ambiguity when conducting IOD with Topocentric Intersection Theory Analysis is increased when considering measurement uncertainty. What are previously single point intersections in the admissible region, ideally, become areas of intersection when uncertainty is considered [13]. To study this effect, we consider uncertainty by adding Gaussian noise to the initial and final measurements, sampled from a covariance matrix representing the measurement uncertainty of the simulated observer. The measured variables are assumed to be independent and uncorrelated, resulting in a diagonal matrix.

The uncertainty values are analytically approximated with equations given in [9], where variance in the angle measurement is

$$\sigma_{\alpha_0} \sim \frac{3\sigma_\alpha}{2\sqrt{N}} \tag{3}$$

and in the angle-rate measurement is

$$\sigma_{\dot{\alpha}_0} \sim \frac{2\sqrt{3}\sigma_\alpha}{T\sqrt{N}} \tag{4}$$

In these equations, the variable N is the number of images or observations that comprise the full linear streak producing the attributable vector. The variable T is the time span over which these observations are taken. For this work, the observations are taken to consist of two images over a one-minute time span, giving $N = 2$ and $T = 60$ seconds. The variable σ_α is the uncertainty in the sensor itself, and we use values of $\sigma_\alpha = 0.1$ arcsecond and $\sigma_\alpha = 0.01$ arcseconds to explore the effects of varying levels of uncertainty. Since the angle-rate uncertainty is a function of time as well, the general structure of the covariance matrices includes a relatively small angle uncertainty with an angle-rate uncertainty several orders of magnitude higher, especially when considering that the variable T must be non-dimensionalized for the CR3BP.

To understand how uncertainty affects the measurement residual contour, we repeat the generation process 1000 times for each observation scenario. A single run consists of its own set of virtual objects, and thus its own set of measurement residual vectors. The measurement residual vectors are then averaged at each initial range and range-rate pairing, then their norms are taken to produce a new contour of the measurement residual. This contour captures the averaged expected behavior when measurement uncertainty is considered in both the initial and final measurements.

An example of this result is shown in Fig. 5, where the top row of figures depicts the averaged results for $\sigma_\alpha = 0.1$ arcsecond and the bottom row depicts $\sigma_\alpha = 0.01$ arcseconds. The averaged measurement residual contour considering uncertainty is shown as an overlay in solid lines to the original from the perfect measurements in dotted lines. A general pattern in these results is the shifting minima along the range-rate direction, even when the structure in the range direction remains relatively unchanged. An example of this is shown in Fig. 5e, where the two local minima appear to be in the same range location, but shifted in the negative range-rate direction. An extreme of this behavior is also observed, where the minima appear to shift outside the bounded initial range and range-rate values, as seen in

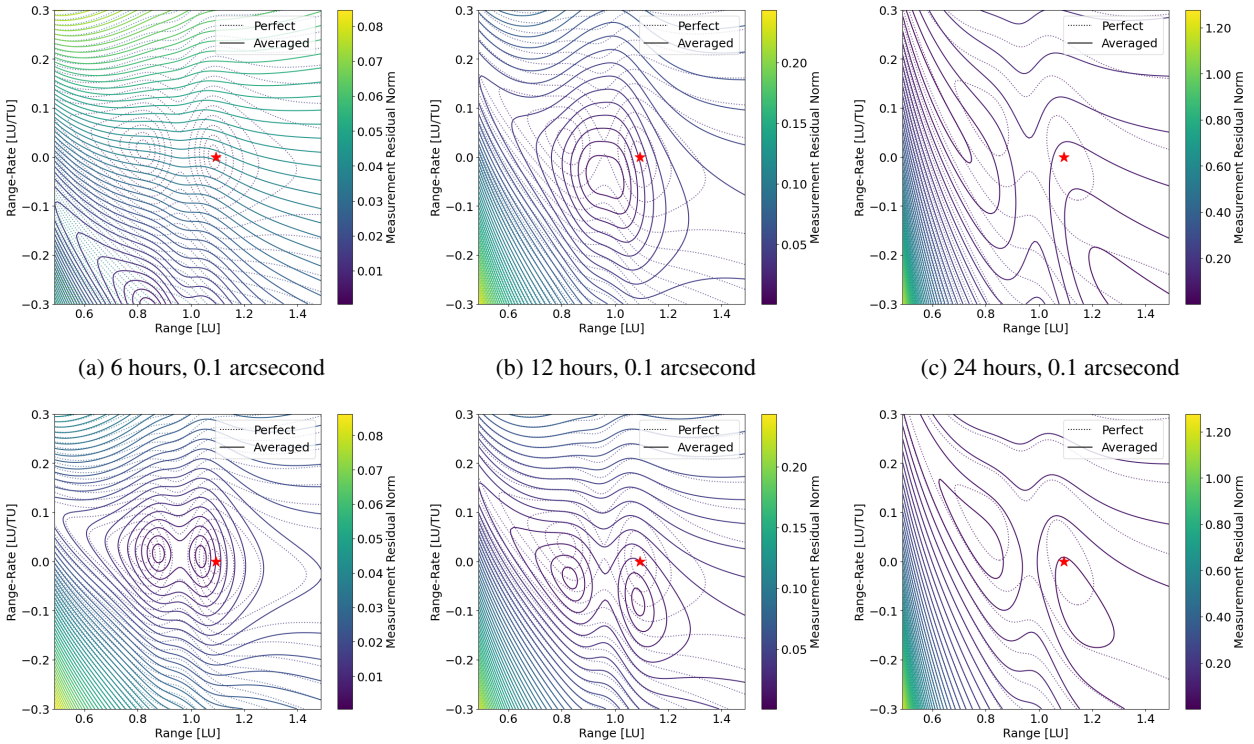

(a) 6 hours, 0.1 arcsecond (b) 12 hours, 0.1 arcsecond (c) 24 hours, 0.1 arcsecond

(d) 6 hours, 0.01 arcsecond (e) 12 hours, 0.01 arcsecond (f) 24 hours, 0.01 arcsecond

Fig. 5: Sample measurement residual contour shifts for two levels of uncertainty.

Fig. 5a. One other major pattern is the combination of what was previously two distinct local minima into one global minimum, as shown in Fig. 5b.

The results for all observation scenarios are shown in the Appendix in Section 7, following the composite contour line and measurement residual contour plots from the perfect observation scenario. The figures are grouped by initial point along the orbit, with the rows depicting the two levels of uncertainty and the columns showing time between measurements. We see that with long enough measurement intervals, it is possible to reattain two distinct local minima, even though they are shifted in the range-rate direction. Additionally, we observe a weakness in the data along the range-rate, due to the greater uncertainty level in that direction compared to the range.

4. CONCLUSION

This work develops an extension of Intersection Theory Analysis to the CR3BP dynamics of cislunar space using measurement and sensor-centric admissible regions, and applies it to three L2 orbits of interest: the planar orbit that connects to the halo family, a halo orbit with 3:1 resonance, and a Near-Rectilinear Halo Orbit with 9:2 resonance. The result is a visual method of conducting IOD with two measurements, which also serves as a method of generating initial guesses for more sophisticated algorithms. With an initial attributable vector and hypothesized range and range-rate values from a linear grid sampling, a field of virtual objects is generated and propagated forward for the time between measurements. The predicted measurements of the virtual objects are then compared to the final measurement to isolate the sets of initial range and range-rate values that produce the correct value for each measured variable. In other words, we generate lower dimensional projections of the two-dimensional admissible region embedded in six-dimensional phase space. When plotted, the intersection of the projections indicates the true initial range and range-rate. We reinterpret the projections of the admissible region as contours of the measurement residual, where the minimum points towards the true initial range and range-rate. There consistently appears to be an ambiguous solution, though, located along the line of sight. When considering the effects of uncertainty, we notice that the minima shift in the initial range and range-rate plane. The results exhibit a weakness in the range-rate direction, attributed to the

greater uncertainty for that variable.

There are some limitations with this current approach. One is the dependence on numerical precision for the results, especially when considering shorter time intervals between measurements. With shorter time scales, the spread of values for a particular variable after propagation can be relatively small, thus allowing the location of the contour line to shift significantly when isolating ta singular value. With longer time horizons, the overall spread of values increases, resulting in a more distinct projection for each measured variable and thus more distinct intersections. Another limitation is the existence of ambiguous solutions, whether looking at the projections of the admissible region or reinterpreting them as a contour plot of the measurement residual. It is expected that the global minima of the measurement residual corresponds to the true initial range and range-rate, but when considering just the measurement information, there are ambiguous solutions due to observation geometry. This will be addressed when introducing a third correlated observation, but with only two, there need to be additional constraints on the solution space.

Several avenues for future work exist to address the limitations and also advance the work towards higher fidelity. One example is incorporating relative motion between observers and targets, which introduces the challenge of removing the observer's motion from the measurements before trying to conduct topocentric intersection theory analysis. Another avenue is exploring different visualization methods for the process, especially those that have less numerical dependence. The contour plots and lines used in this work rely heavily on interpolation for plotting and isolating particular values from each grid, but this lowered the precision in the intersection finding process. Other possibilities include finding more effective ways of dividing and sampling the range and range-rate space, rather than using a linear grid sampling. With an intelligently sampled initial range and range-rate space, the number of objects to analyze is reduced, thus reducing the overall computational load.

5. ACKNOWLEDGEMENTS

This work was funded by the Air Force Research Laboratory under contract number FA943-22-2-0050.

6. REFERENCES

[1] David A. Vallado. *Fundamentals of Astrodynamics and Applications*. Microcosm Press, 2001.

[2] Andrea Milani, Giovanni F. Gronchi, Mattia De' Michieli Vitturi, and Zoran Knežević. Orbit determination with very short arcs. I admissible regions. *Celestial Mechanics and Dynamical Astronomy*, 90(1):57–85, September 2004.

[3] G. Tommei, A. Milani, and A. Rossi. Orbit determination of space debris: Admissible regions. *Celestial Mechanics and Dynamical Astronomy*, 97(4):289–304, April 2007.

[4] Davide Farnocchia, Giacomo Tommei, Andrea Milani, and Alessandro Rossi. Innovative methods of correlation and orbit determination for space debris. *Celestial Mechanics and Dynamical Astronomy*, 107(1-2):169–185, June 2010.

[5] Kohei Fujimoto and Daniel J. Scheeres. Applications of the admissible region to space-based observations. *Advances in Space Research*, 52(4):696–704, August 2013.

[6] Sam Wishnek, Marcus J Holzinger, and Patrick Handley. Robust Cislunar Initial Orbit Determination. page 16, 2021.

[7] Paul Billings, Jason Baldwin, Charles J Wetterer, John Gaebler, Christopher Craft, Micah Dilley, Keric Hill, and Jill Bruer. Cislunar initial orbit determination using CAR-MHF. 2023.

[8] Andrea Milani, Giovanni F. Gronchi, Zoran Knežević, Maria Eugenia Sansaturio, and Oscar Arratia. Orbit determination with very short arcs: II. Identifications. *Icarus*, 179(2):350–374, December 2005.

[9] Jared M. Maruskin, Daniel J. Scheeres, and Kyle T. Alfriend. Correlation of Optical Observations of Objects in Earth Orbit. *Journal of Guidance Control and Dynamics*, 32(1):194–209, January 2009.

[10] K. Fujimoto and D. J. Scheeres. Correlation of Optical Observations of Earth-Orbiting Objects and Initial Orbit Determination. *Journal of Guidance, Control, and Dynamics*, 35(1):208–221, January 2012.

[11] E. J. Doedel, V. A. Romanov, R. C. Paffenroth, H. B. Keller, D. J. Dichmann, J. Galán-Vioque, and A. Vanderbauwhede. Elemental periodic orbits associated with the libration points in the circular restricted 3-body problem. *International Journal of Bifurcation and Chaos*, 17(08):2625–2677, August 2007.

[12] Diane C Davis, Brian P McCarthy, and Emily M Zimovan-Spreen. PERTURBATIONS AND RECOVERY IN THE GATEWAY NEAR RECTILINEAR HALO ORBIT.

[13] Johnny L. Worthy and Marcus J. Holzinger. Incorporating Uncertainty in Admissible Regions for Uncorrelated Detections. *Journal of Guidance, Control, and Dynamics*, 38(9):1673–1689, September 2015.

7. APPENDIX

7.1 Halo Orbit (3:1 Resonance) Figures

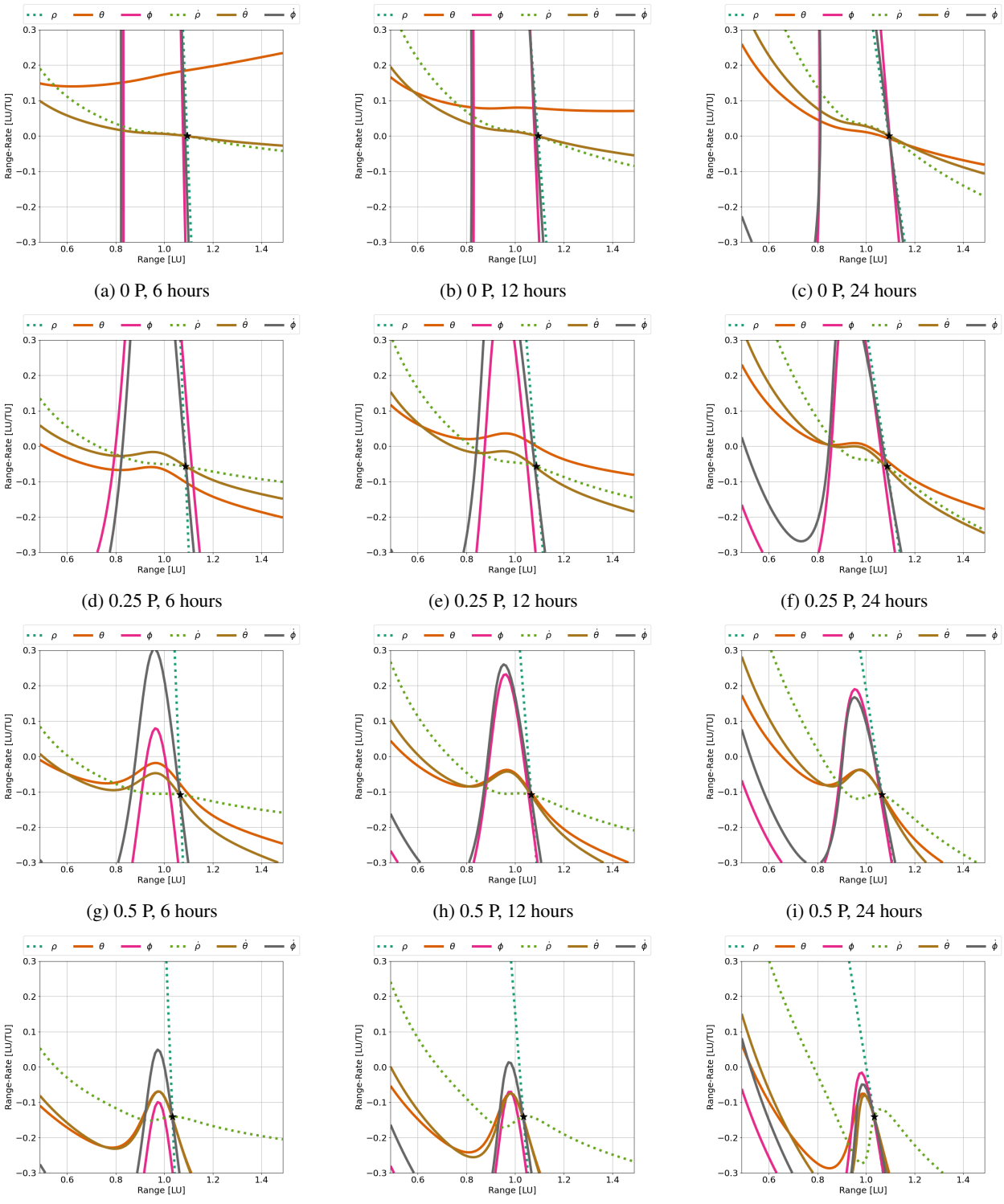

(a) 0 P, 6 hours (b) 0 P, 12 hours (c) 0 P, 24 hours

(d) 0.25 P, 6 hours (e) 0.25 P, 12 hours (f) 0.25 P, 24 hours

(g) 0.5 P, 6 hours (h) 0.5 P, 12 hours (i) 0.5 P, 24 hours

(j) 0.75 P, 6 hours (k) 0.75 P, 12 hours (l) 0.75 P, 24 hours

Fig. 6: Composite intersection plots for Halo orbit (3:1 Resonance). Rows indicate initial measurement along orbit and columns indicate time between measurements. Black star shows true initial range and range-rate.

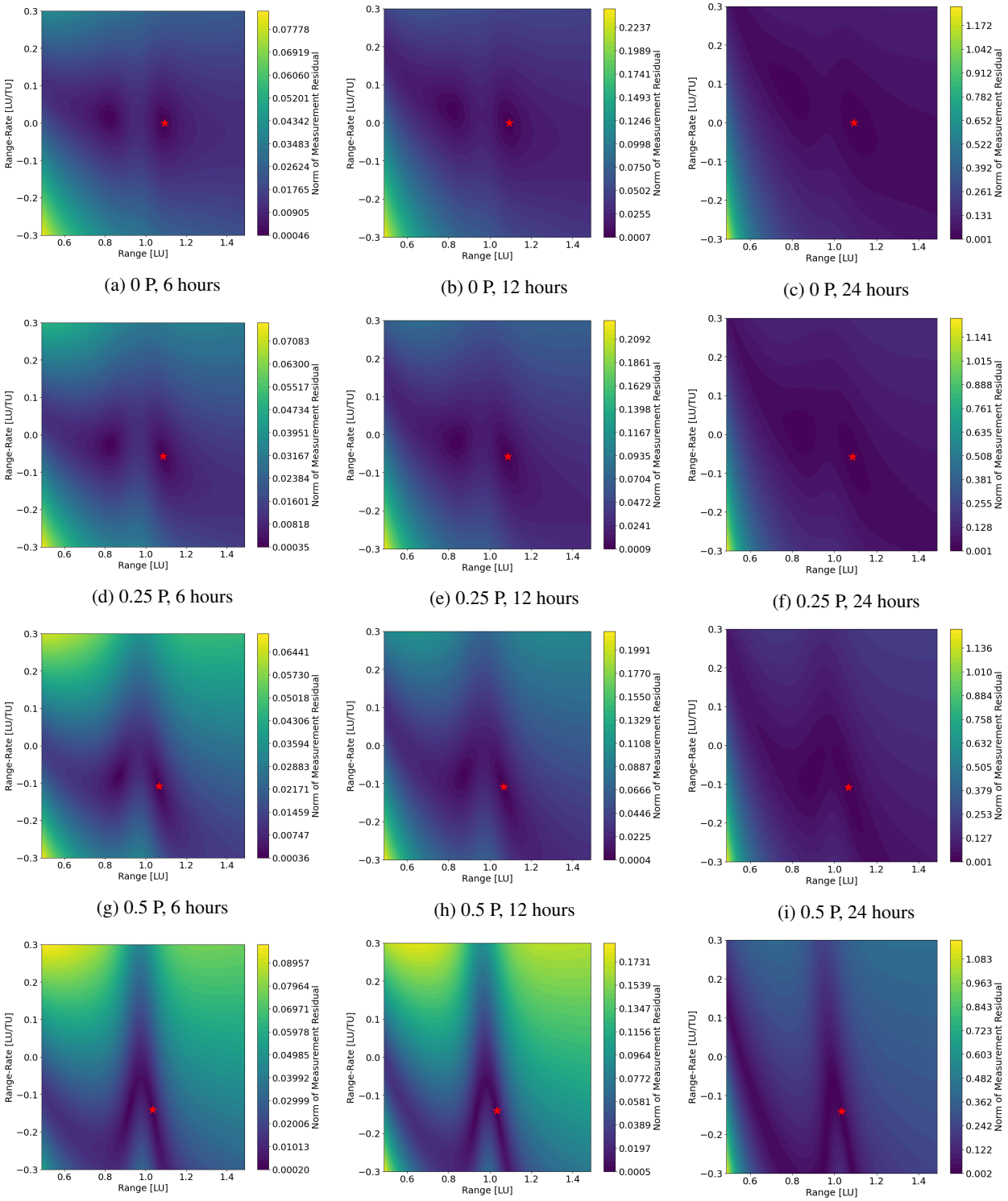

(a) 0 P, 6 hours (b) 0 P, 12 hours (c) 0 P, 24 hours

(d) 0.25 P, 6 hours (e) 0.25 P, 12 hours (f) 0.25 P, 24 hours

(g) 0.5 P, 6 hours (h) 0.5 P, 12 hours (i) 0.5 P, 24 hours

(j) 0.75 P, 6 hours (k) 0.75 P, 12 hours (l) 0.75 P, 24 hours

Fig. 7: Measurement residual contour plots for Halo orbit (3:1 Resonance). Rows indicate initial measurement along orbit and columns indicate time between measurements. Red star shows true initial range and range-rate.

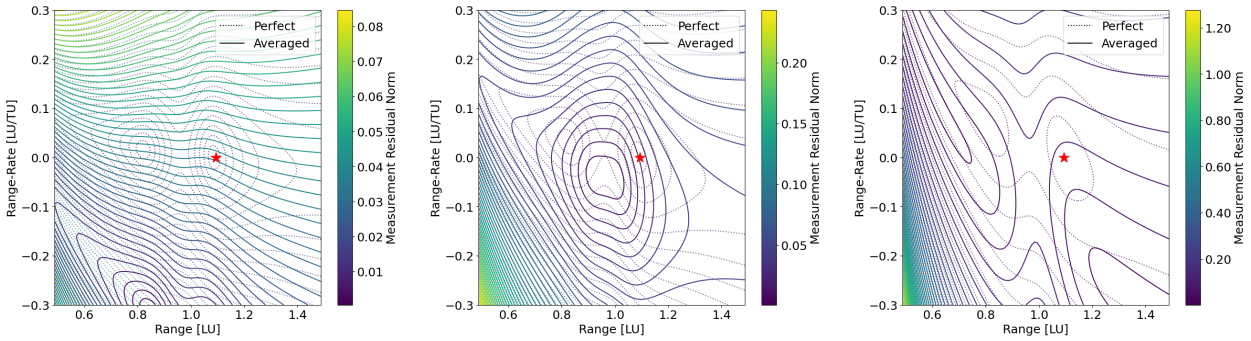

(a) 6 hours, 0.1 arcsecond (b) 12 hours, 0.1 arcsecond (c) 24 hours, 0.1 arcsecond

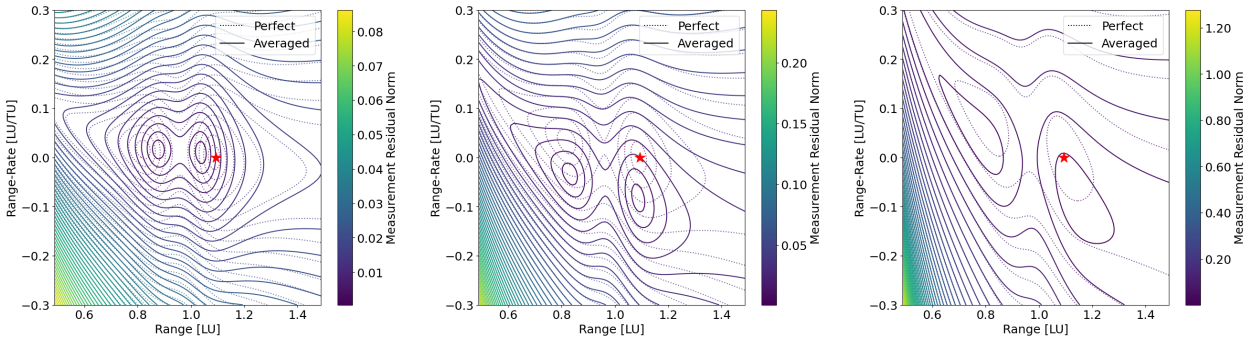

(d) 6 hours, 0.01 arcsecond (e) 12 hours, 0.01 arcsecond (f) 24 hours, 0.01 arcsecond

Fig. 8: Contour shifts for initial condition at 0 P for Halo orbit (3:1 Resonance).

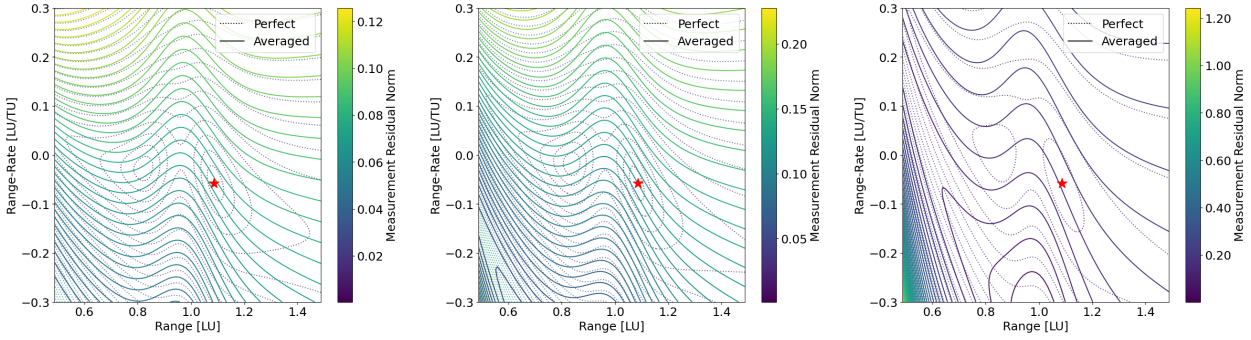

(a) 6 hours, 0.1 arcsecond (b) 12 hours, 0.1 arcsecond (c) 24 hours, 0.1 arcsecond

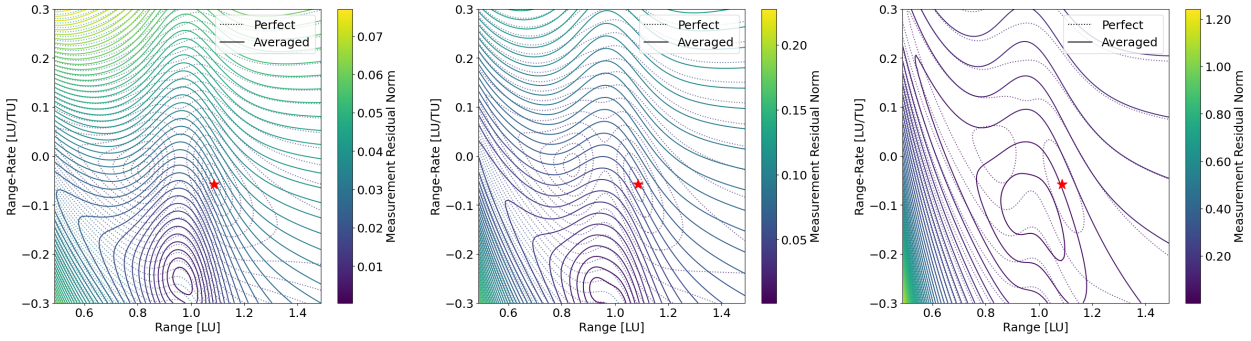

(d) 6 hours, 0.01 arcsecond (e) 12 hours, 0.01 arcsecond (f) 24 hours, 0.01 arcsecond

Fig. 9: Contour shifts for initial condition at 0.25 P for Halo orbit (3:1 Resonance).

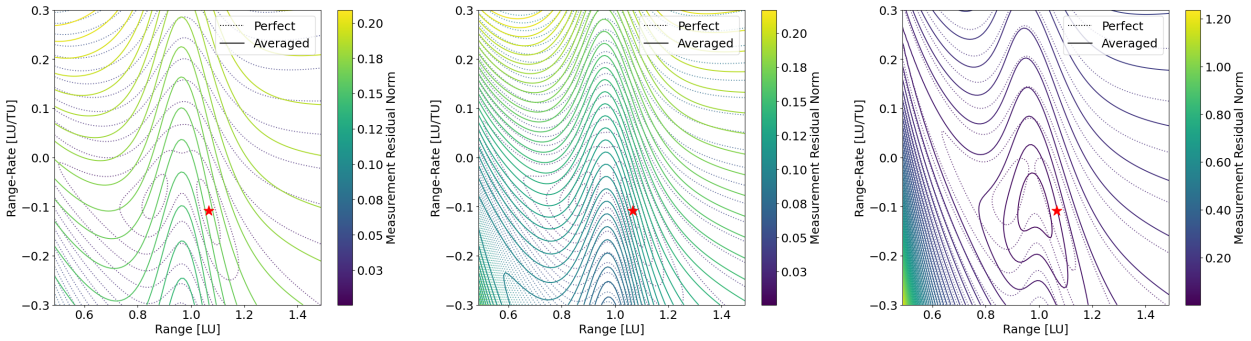

(a) 6 hours, 0.1 arcsecond (b) 12 hours, 0.1 arcsecond (c) 24 hours, 0.1 arcsecond

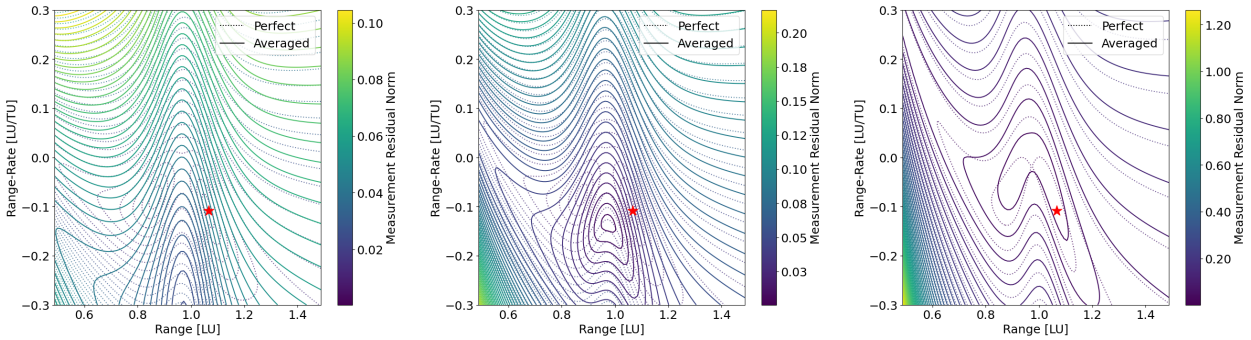

(d) 6 hours, 0.01 arcsecond (e) 12 hours, 0.01 arcsecond (f) 24 hours, 0.01 arcsecond

Fig. 10: Contour shifts for initial condition at 0.50 P for Halo orbit (3:1 Resonance).

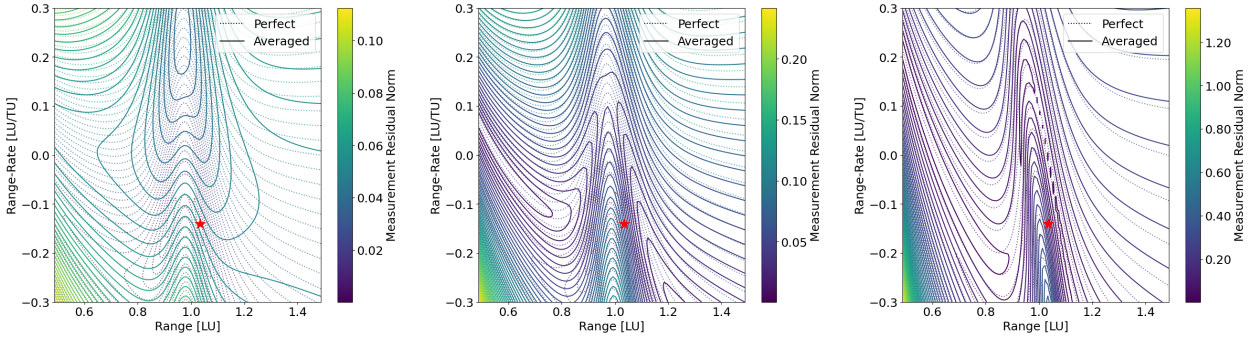

(a) 6 hours, 0.1 arcsecond (b) 12 hours, 0.1 arcsecond (c) 24 hours, 0.1 arcsecond

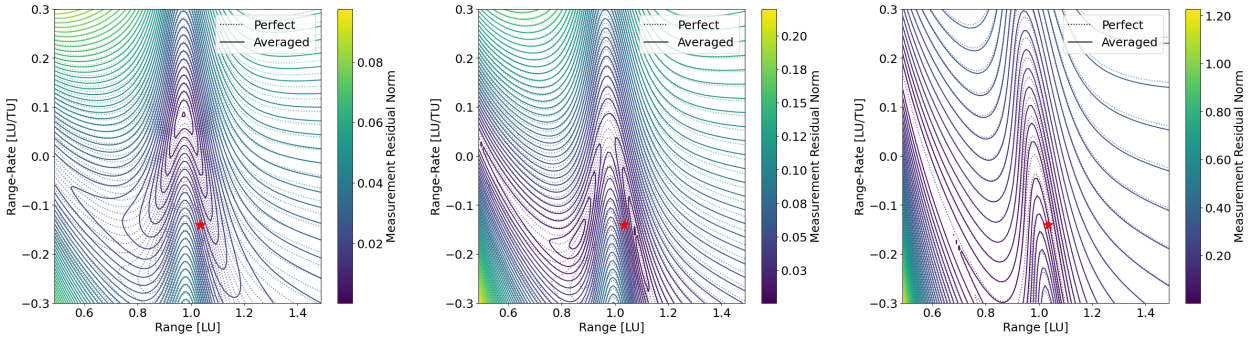

(d) 6 hours, 0.01 arcsecond (e) 12 hours, 0.01 arcsecond (f) 24 hours, 0.01 arcsecond

Fig. 11: Contour shifts for initial condition at 0.75 P for Halo orbit (3:1 Resonance).

7.2 Planar Orbit Figures

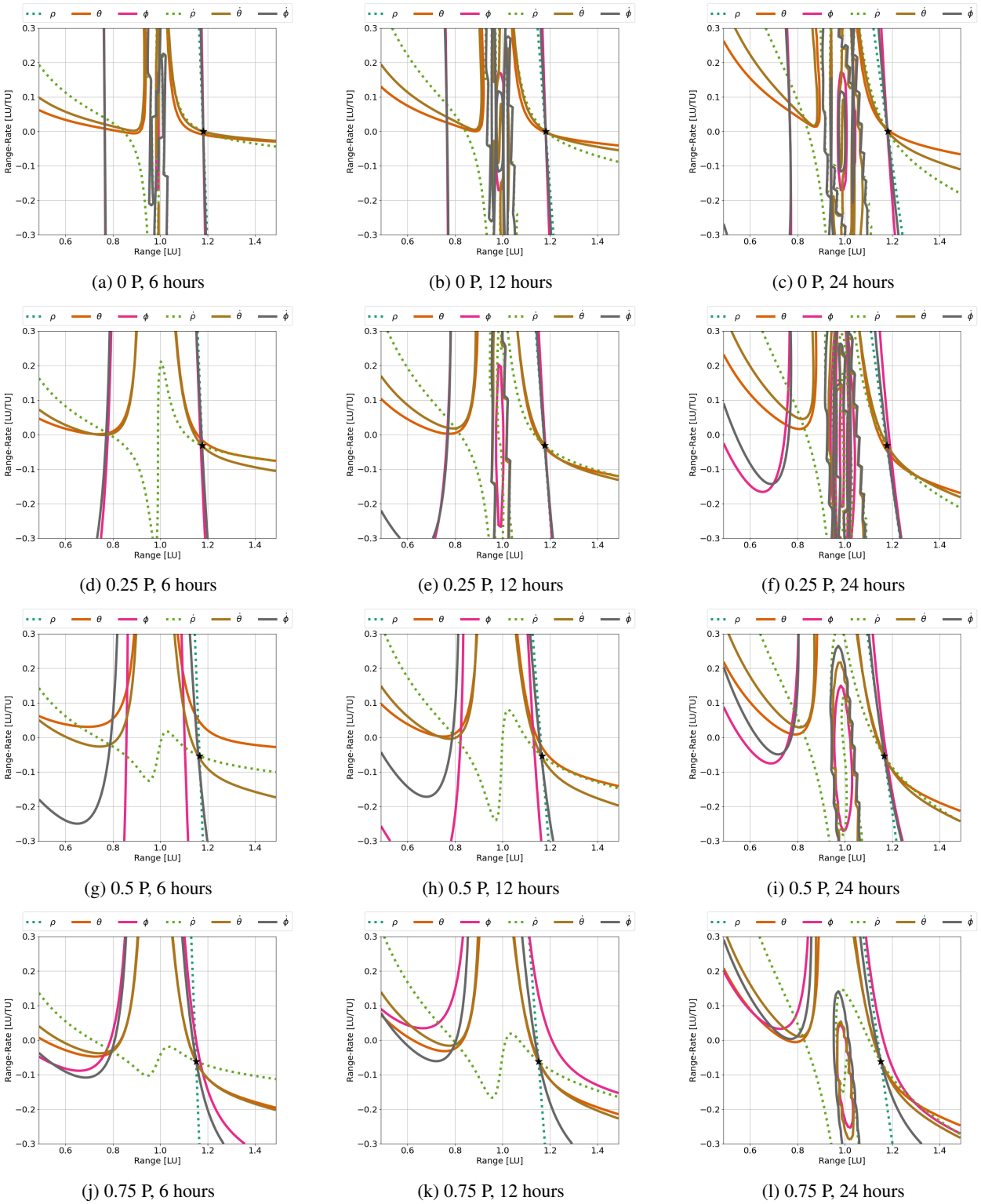

(a) 0 P, 6 hours (b) 0 P, 12 hours (c) 0 P, 24 hours

(d) 0.25 P, 6 hours (e) 0.25 P, 12 hours (f) 0.25 P, 24 hours

(g) 0.5 P, 6 hours (h) 0.5 P, 12 hours (i) 0.5 P, 24 hours

(j) 0.75 P, 6 hours (k) 0.75 P, 12 hours (l) 0.75 P, 24 hours

Fig. 12: Composite intersection plots for planar orbit. Rows indicate initial measurement along orbit and columns indicate time between measurements. Black star shows true initial range and range-rate.

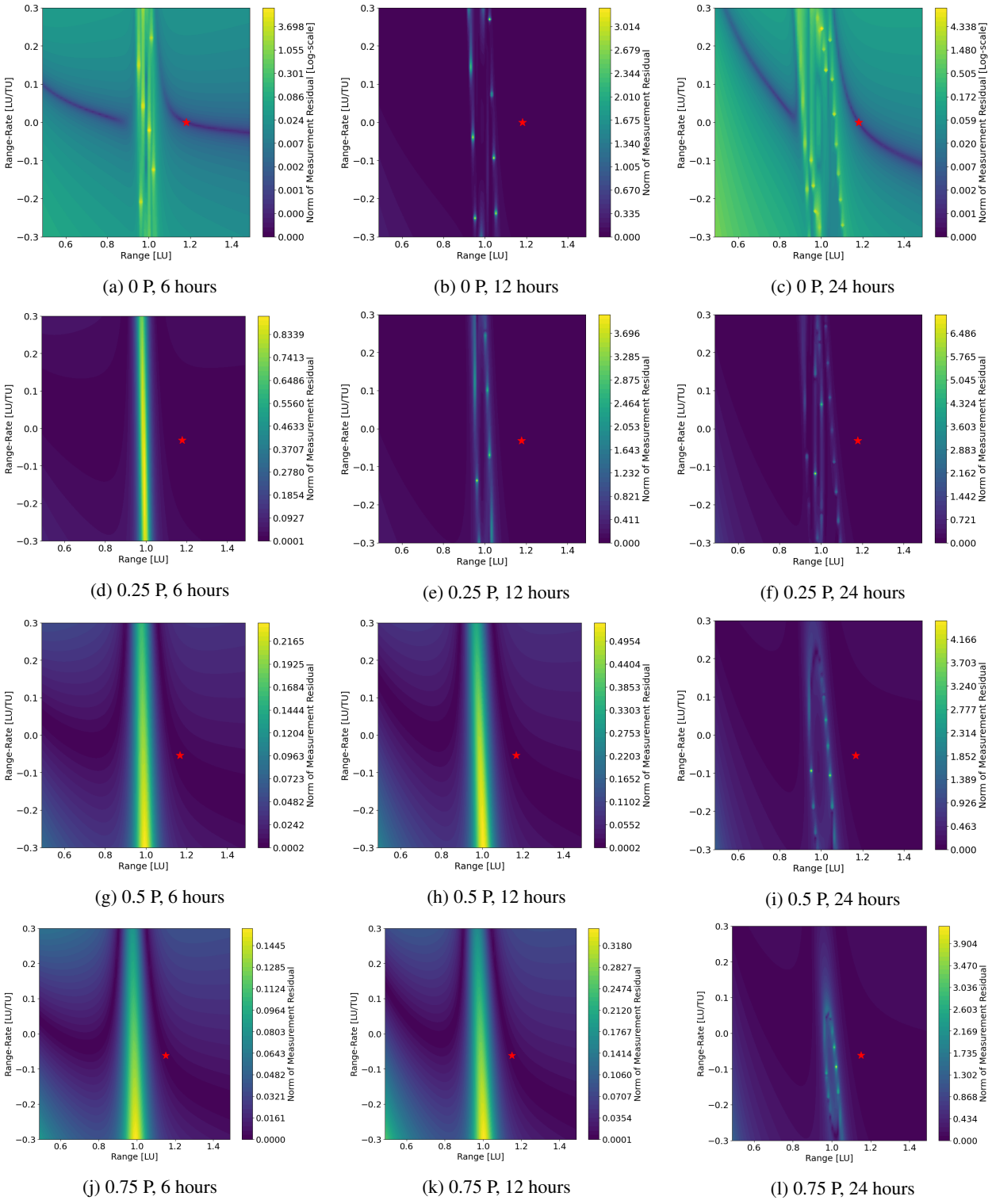

(a) 0 P, 6 hours (b) 0 P, 12 hours (c) 0 P, 24 hours

(d) 0.25 P, 6 hours (e) 0.25 P, 12 hours (f) 0.25 P, 24 hours

(g) 0.5 P, 6 hours (h) 0.5 P, 12 hours (i) 0.5 P, 24 hours

(j) 0.75 P, 6 hours (k) 0.75 P, 12 hours (l) 0.75 P, 24 hours

Fig. 13: Measurement residual contour plots for planar orbit. Rows indicate initial measurement along orbit and columns indicate time between measurements. Red star shows true initial range and range-rate.

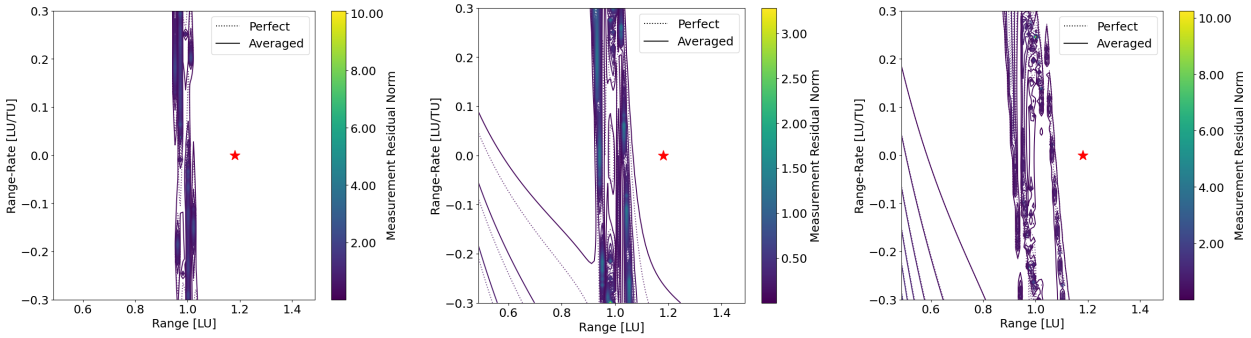

(a) 6 hours, 0.1 arcsecond (b) 12 hours, 0.1 arcsecond (c) 24 hours, 0.1 arcsecond

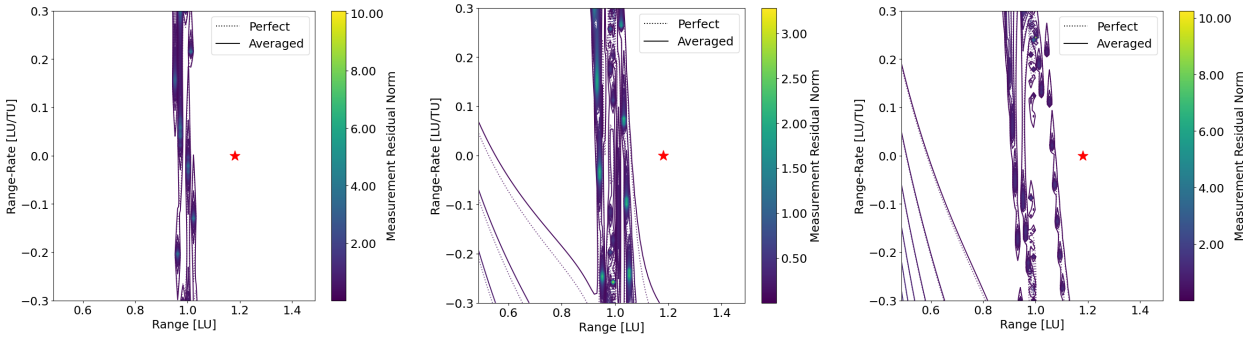

(d) 6 hours, 0.01 arcsecond (e) 12 hours, 0.01 arcsecond (f) 24 hours, 0.01 arcsecond

Fig. 14: Contour shifts for initial condition at 0 P for planar orbit.

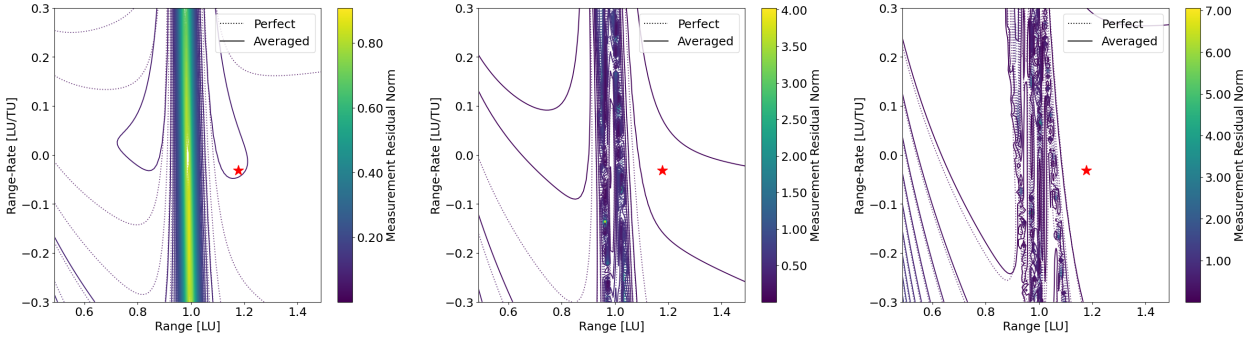

(a) 6 hours, 0.1 arcsecond (b) 12 hours, 0.1 arcsecond (c) 24 hours, 0.1 arcsecond

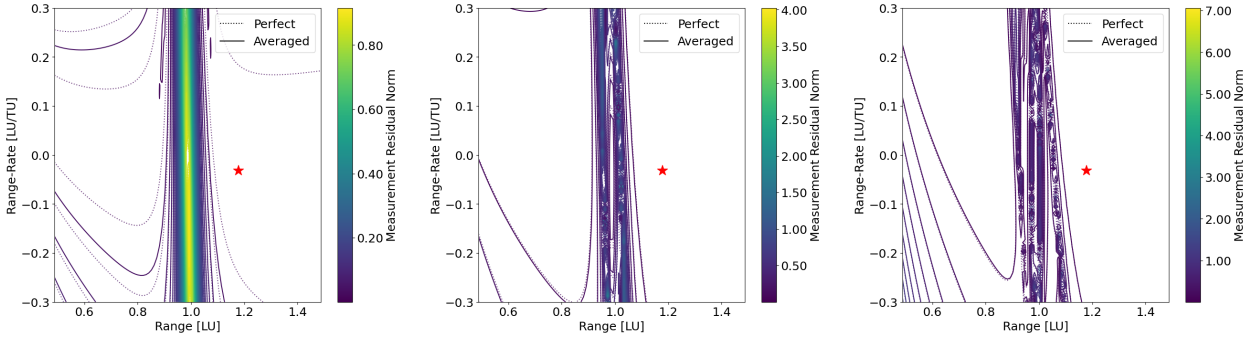

(d) 6 hours, 0.01 arcsecond (e) 12 hours, 0.01 arcsecond (f) 24 hours, 0.01 arcsecond

Fig. 15: Contour shifts for initial condition at 0.25 P for planar orbit.

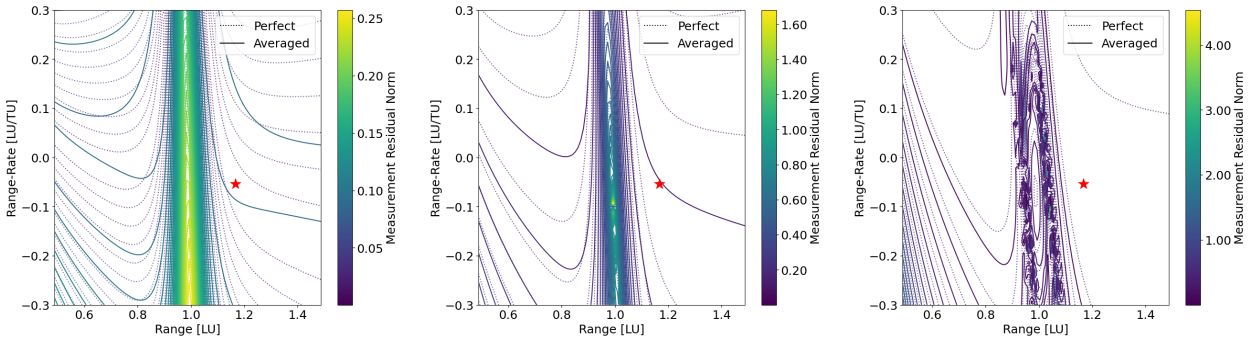

(a) 6 hours, 0.1 arcsecond (b) 12 hours, 0.1 arcsecond (c) 24 hours, 0.1 arcsecond

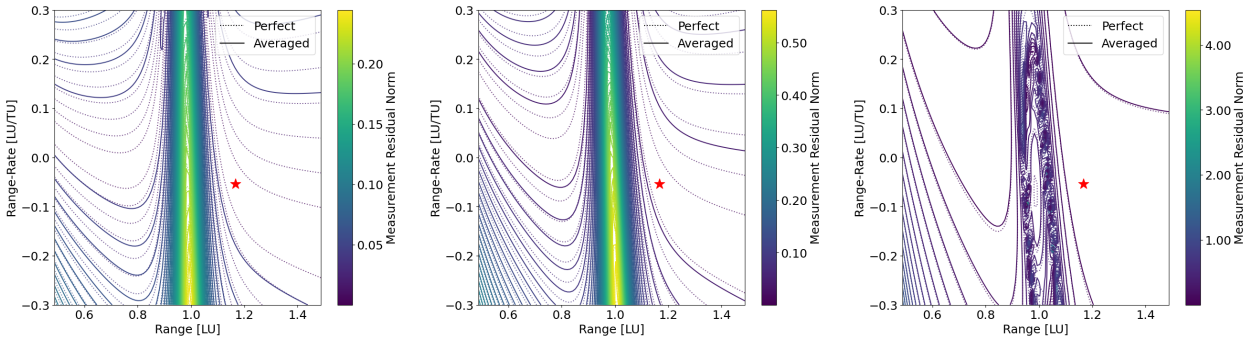

(d) 6 hours, 0.01 arcsecond (e) 12 hours, 0.01 arcsecond (f) 24 hours, 0.01 arcsecond

Fig. 16: Contour shifts for initial condition at 0.50 P for planar orbit.

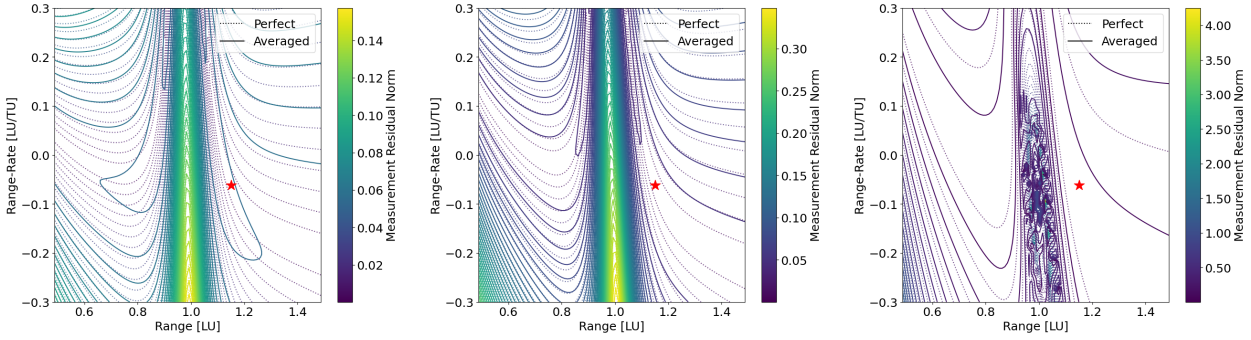

(a) 6 hours, 0.1 arcsecond (b) 12 hours, 0.1 arcsecond (c) 24 hours, 0.1 arcsecond

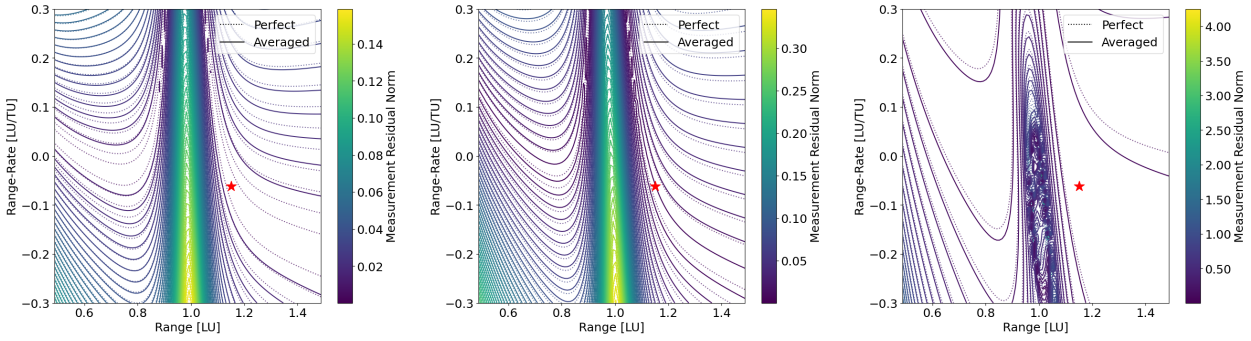

(d) 6 hours, 0.01 arcsecond (e) 12 hours, 0.01 arcsecond (f) 24 hours, 0.01 arcsecond

Fig. 17: Contour shifts for initial condition at 0.75 P for planar orbit.

7.3 Near-Rectilinear Halo Orbit (9:2 Resonance) Figures

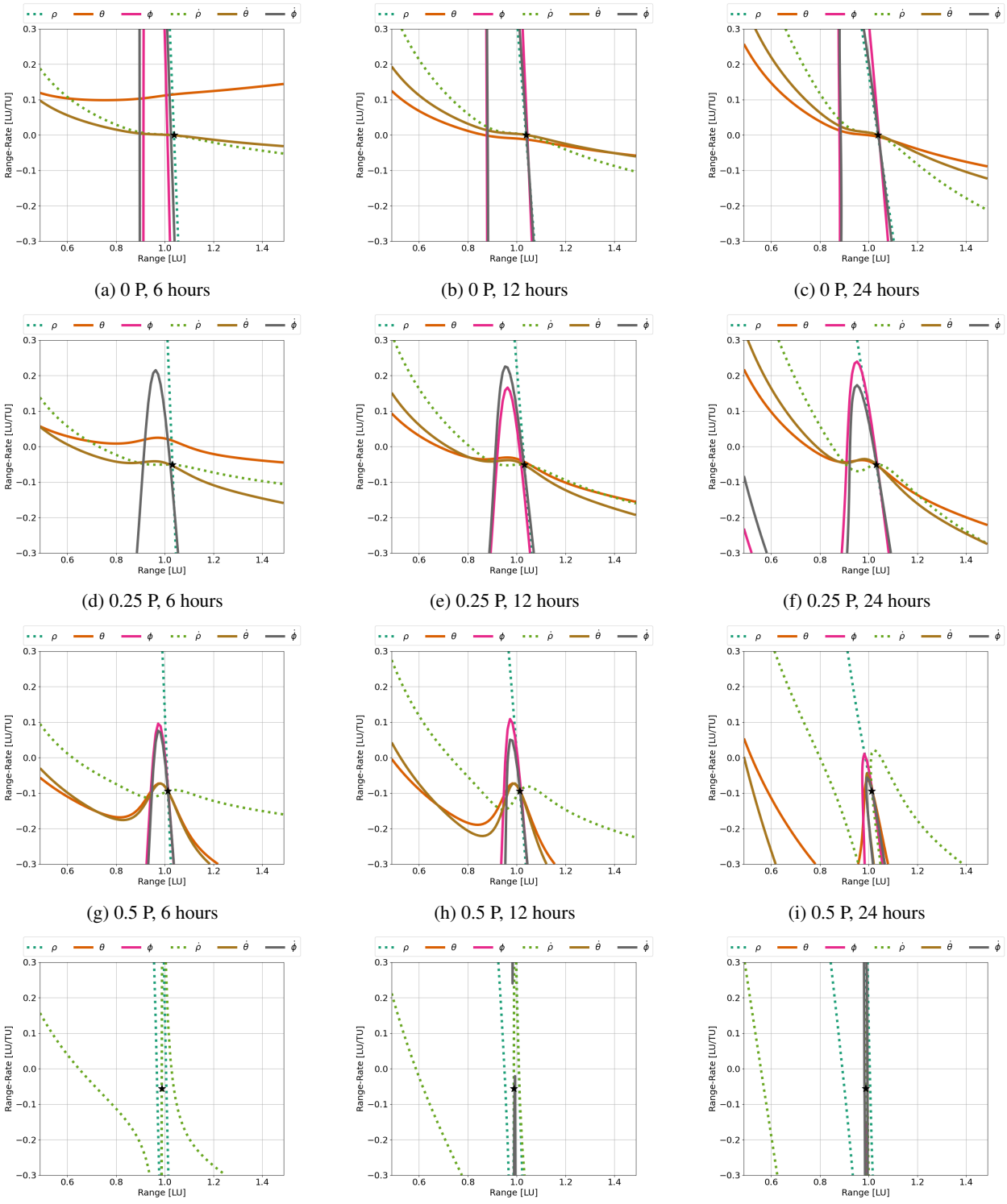

(a) 0 P, 6 hours (b) 0 P, 12 hours (c) 0 P, 24 hours

(d) 0.25 P, 6 hours (e) 0.25 P, 12 hours (f) 0.25 P, 24 hours

(g) 0.5 P, 6 hours (h) 0.5 P, 12 hours (i) 0.5 P, 24 hours

(j) 0.75 P, 6 hours (k) 0.75 P, 12 hours (l) 0.75 P, 24 hours

Fig. 18: Composite intersection plots for Near-Rectilinear Halo Orbit (9:2 Resonance). Rows indicate initial measurement along orbit and columns indicate time between measurements. Black star shows true initial range and range-rate.

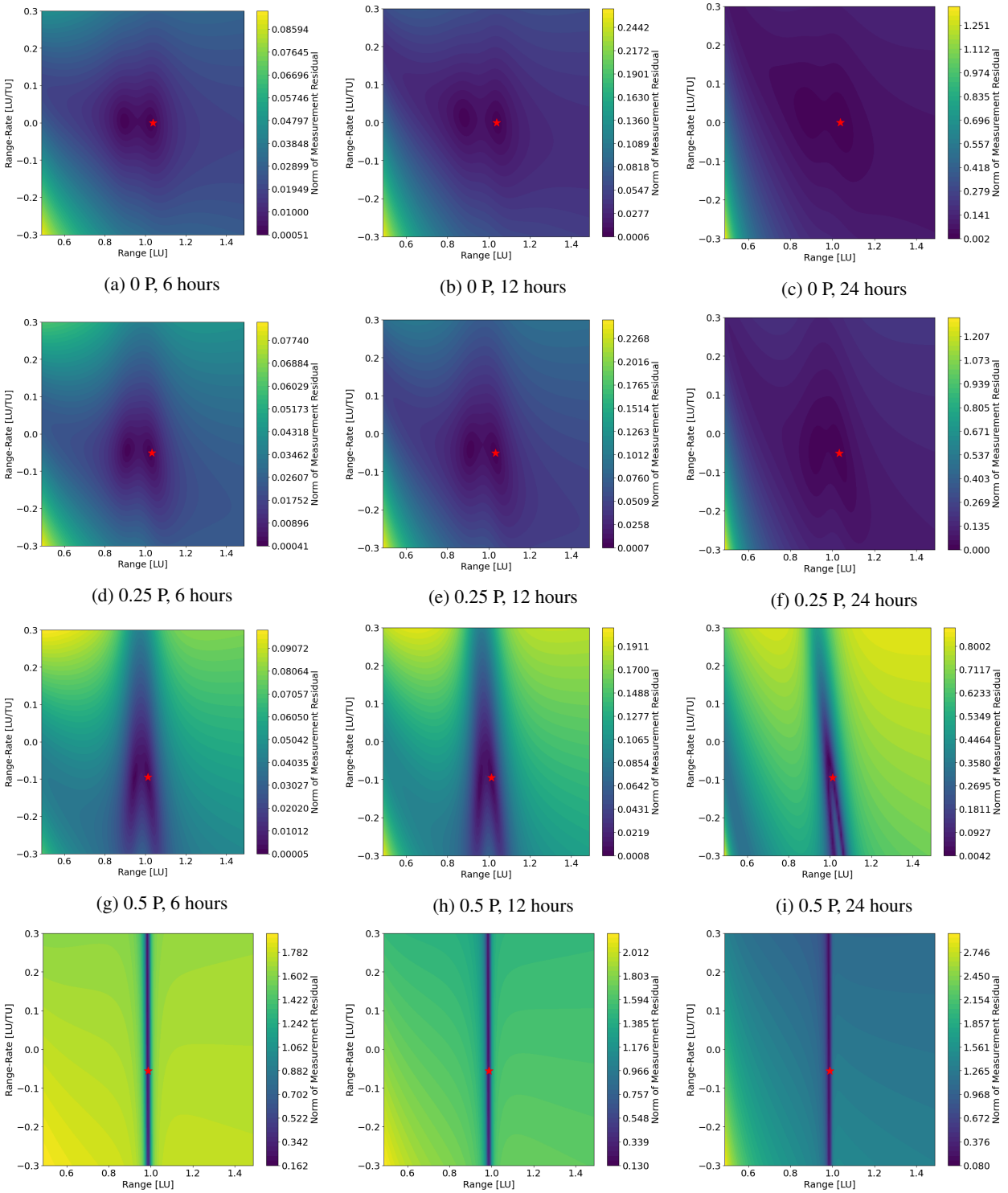

(a) 0 P, 6 hours (b) 0 P, 12 hours (c) 0 P, 24 hours

(d) 0.25 P, 6 hours (e) 0.25 P, 12 hours (f) 0.25 P, 24 hours

(g) 0.5 P, 6 hours (h) 0.5 P, 12 hours (i) 0.5 P, 24 hours

(j) 0.75 P, 6 hours (k) 0.75 P, 12 hours (l) 0.75 P, 24 hours

Fig. 19: Measurement residual contour plots for Near-Rectilinear Halo Orbit (9:2 Resonance). Rows indicate initial measurement along orbit and columns indicate time between measurements. Red star shows true initial range and range-rate.

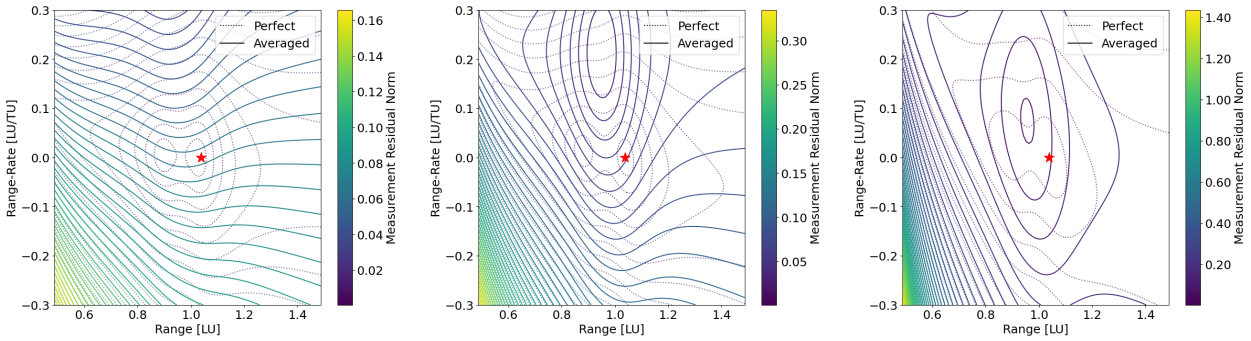

(a) 6 hours, 0.1 arcsecond (b) 12 hours, 0.1 arcsecond (c) 24 hours, 0.1 arcsecond

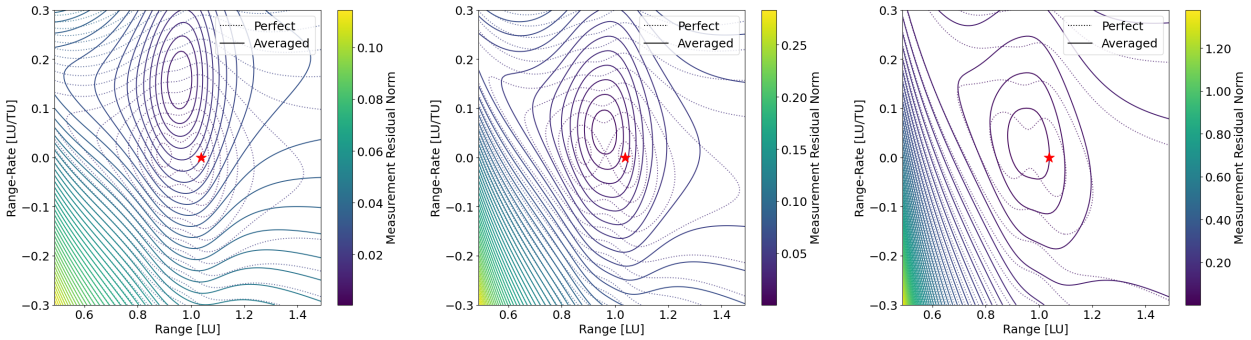

(d) 6 hours, 0.01 arcsecond (e) 12 hours, 0.01 arcsecond (f) 24 hours, 0.01 arcsecond

Fig. 20: Contour shifts for initial condition at 0 P for Near-Rectilinear Halo Orbit (9:2 Resonance).

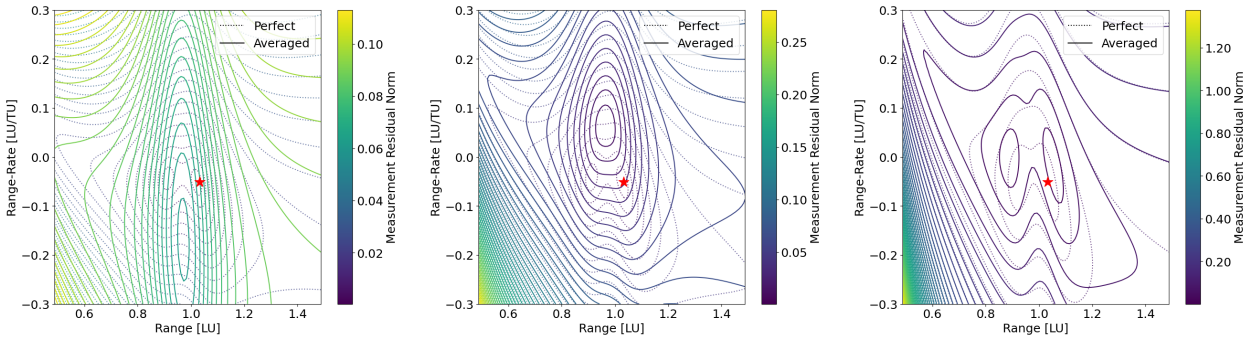

(a) 6 hours, 0.1 arcsecond (b) 12 hours, 0.1 arcsecond (c) 24 hours, 0.1 arcsecond

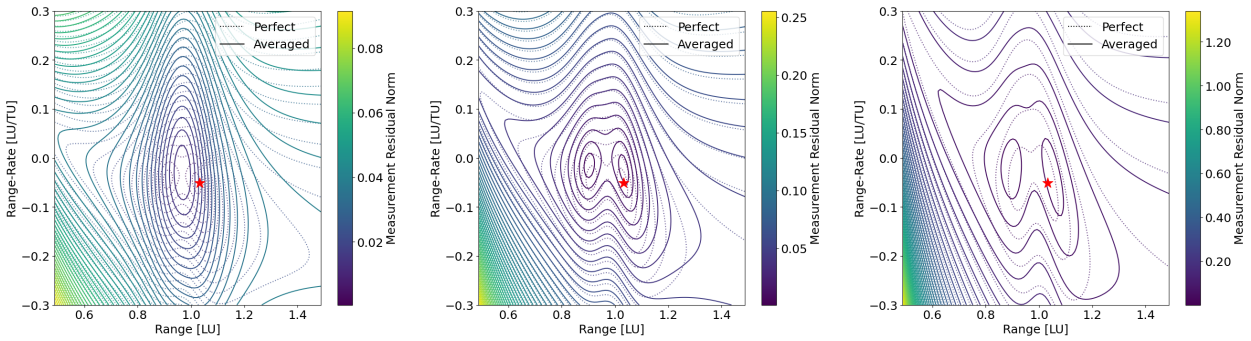

(d) 6 hours, 0.01 arcsecond (e) 12 hours, 0.01 arcsecond (f) 24 hours, 0.01 arcsecond

Fig. 21: Contour shifts for initial condition at 0.25 P for Near-Rectilinear Halo Orbit (9:2 Resonance).

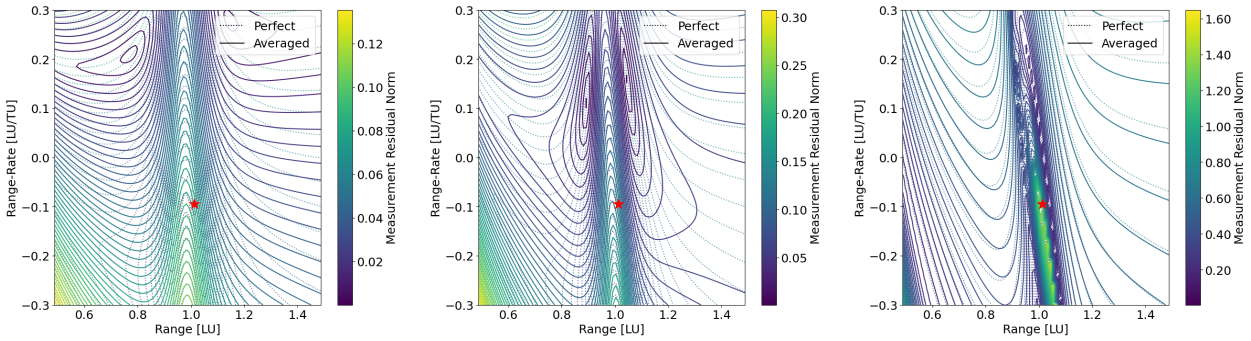

(a) 6 hours, 0.1 arcsecond (b) 12 hours, 0.1 arcsecond (c) 24 hours, 0.1 arcsecond

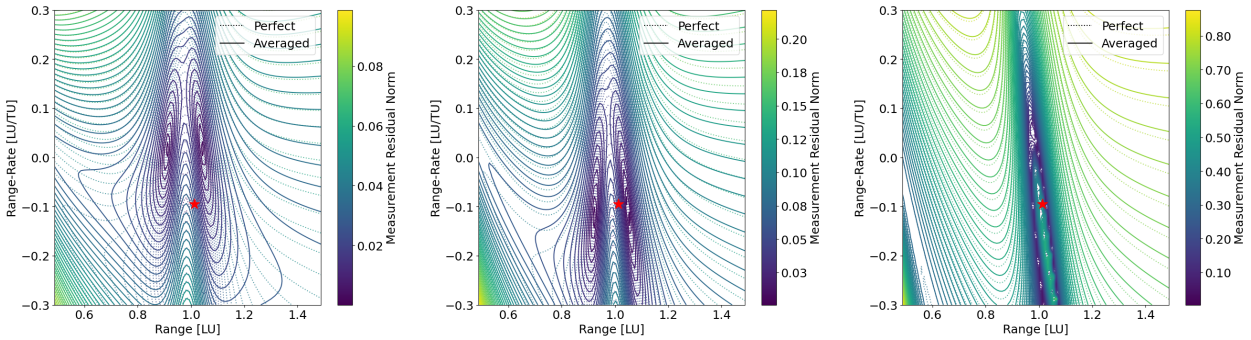

(d) 6 hours, 0.01 arcsecond (e) 12 hours, 0.01 arcsecond (f) 24 hours, 0.01 arcsecond

Fig. 22: Contour shifts for initial condition at 0.50 P for Near-Rectilinear Halo Orbit (9:2 Resonance).

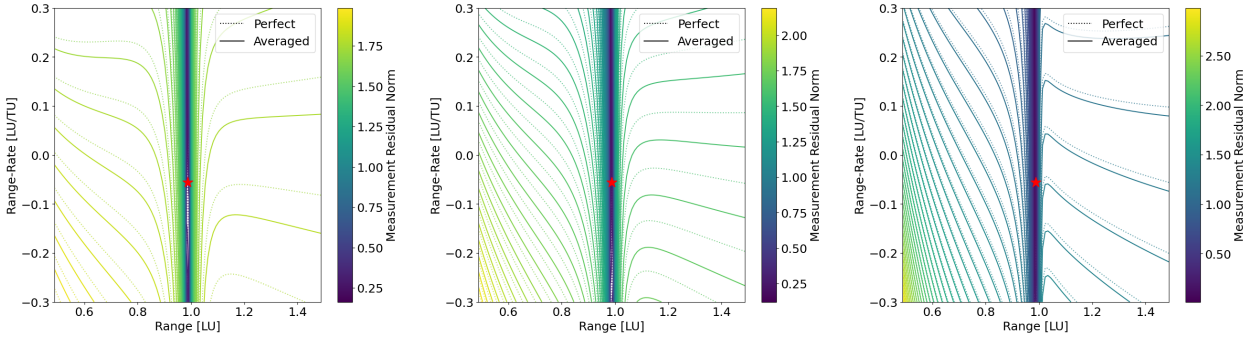

(a) 6 hours, 0.1 arcsecond (b) 12 hours, 0.1 arcsecond (c) 24 hours, 0.1 arcsecond

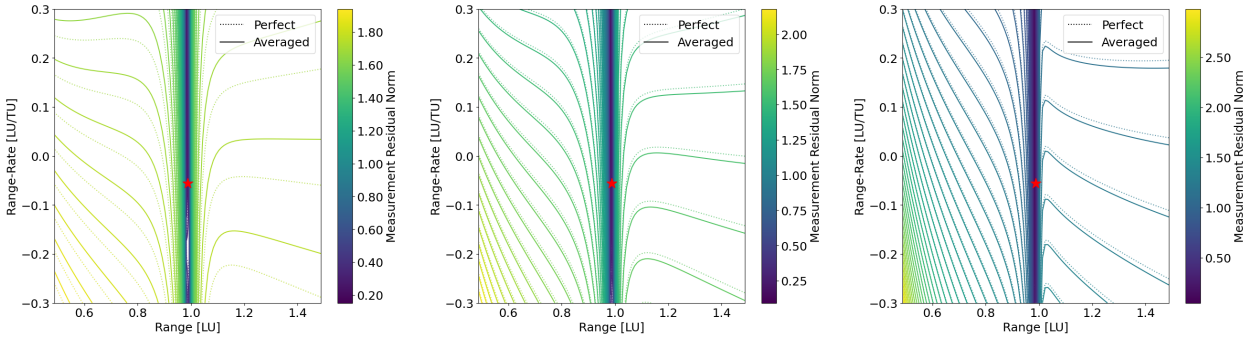

(d) 6 hours, 0.01 arcsecond (e) 12 hours, 0.01 arcsecond (f) 24 hours, 0.01 arcsecond

Fig. 23: Contour shifts for initial condition at 0.75 P for Near-Rectilinear Halo Orbit (9:2 Resonance).